The numerical simulation of Taylor-Couette flow with radial temperature gradient

E Tuliszka-Sznitko and K Kiełczewski

Institute of Thermal Engineering, Poznań University of Technology, Poland

E-mail: ewa.tuliszka-sznitko@put.poznan.pl

Abstract. The Taylor-Couette flow with radial temperature gradient is a canonical problem for the study of heat transfer in engineering issues. However, gaining insight into the transitional Taylor-Couette flow with temperature gradient still requires detailed experimental and numerical investigations. In the present paper we have performed computations for the cavity of aspect ratio $\Gamma = 3.76$ and radii ratios $\eta = 0.82$ and 0.375 with the heated rotating bottom disk and stationary outer cylinder. We analyse the influence of the end-wall boundary conditions and the thermal conditions on the flow structure, and on the distributions of the Nusselt number and torque along the inner and outer cylinders. The averaged values along the inner cylinder of the Nusselt number and torque obtained for different Re are analysed in the light of the results published in [2, 16, 17].

1. Introduction

Transitional flow driven by the combination of the rotation and the thermal gradients determines the dynamics which occur in complex industrial flows. The Taylor-Couette flow is one of paradigmatical systems in hydrodynamics very well suited for studying the primary instability, transitional flows and fully turbulent flows in the varying temperature fields. An overview of issues related to the Taylor-Couette flow with heat transfer can be found in [1, 2]. Regardless of the significance of the problem for basic research, the results obtained for the geometrically simple Taylor-Couette flow can be directly used in designing and optimizing many devices, such as: cooling systems in gas turbines and axial compressors, ventilation installations, desalination tanks and waste water tanks, nuclear reactor fuel rods [3, 4, 5, 6]. The Taylor-Couette flow is governed by the following parameters: radii ratio $\eta = R_1 / R_2$ (where R_1 and R_2 are the radii of the inner and outer cylinders respectively), by curvature parameter $Rm = (R_2 + R_1)/(R_2 - R_1)$ and by aspect ratio $\Gamma = H/(R_2 - R_1)$, where H is the axial dimension of the domain, figure 1. Reynolds number is defined in the following way: $\mathrm{Re} = \Omega(R_2 - R_1)R_1/\nu$ where Ω is the rotation of the inner cylinder and the bottom disk, ν is the kinematic viscosity of the fluid. The heat transfer is characterized by the thermal Rossby number $B = \beta(T_2 - T_1)$, where T_2 and T_1 are temperatures of the heated and cooled walls (β is thermal expansion coefficient).

The literature on the Taylor-Couette flow with heat transfer includes experimental, theoretical and numerical studies [7, 8, 9]. Instability and transitional process in the cavity of large aspect ratio Γ>100 and narrow gap were investigated experimentally, among others, in the papers [10, 11]. The experimental results of the heat transfer obtained in the cavity of aspect ratio Γ= 31.5 ($\eta \sim 0.5$) were published in [12, 13]. The numerical simulations [14] obtained for the cavity of Γ = 10, η = 0.5 delivered detailed information on the flow structure, but the results revealed discrepancies between the

experimental results and numerical ones. These discrepancies were attributed to the influence of the end-wall boundary conditions. The effect of the end-walls was intensively investigated for the isothermal fluid flow in [15], where the authors applied the asymmetric end-wall boundary conditions. In most of the Taylor-Couette flow numerical simulations the assumption of periodicity condition in axial direction has been used. This assumption significantly reduces the computational cost due to the fact that variables can be expanded as a Fourier series in the axial direction, which simplifies the numerical approach. Lopez et al. [2] investigated numerically the heat transfer in fluid flows between rotating cylinders ($5 \leq \Gamma \leq 80$) using no-slip boundary conditions at the end-walls and also, for comparison, using the periodicity condition in axial direction. They showed that the numerical results obtained with the axial periodicity condition agree with those obtained for closed cavities only for small Rayleigh numbers.

In the present paper we analyse the transition process in the Taylor-Couette flow in cavities of small aspect ratio $\Gamma = 3.76$, and radii ratios $\eta = 0.82$ and 0.375 with the heated rotating bottom disk and the heated stationary outer cylinder (the rotating inner cylinder and the stationary top disk are cooled). The Boussinesq approximation is used to take into account the buoyancy effect induced by the involved body forces i.e. the Coriolis force, the circumferential force resulting from the angular velocity of the rotor and the circumferential force, which is caused by the curvature of the particle track. In the paper we analyse the influence of the asymmetric end-wall boundary conditions and the thermal boundary conditions on the flow structure and on the axial and radial distributions of many physical parameters. We focus particularly on the dependence of the Nusselt number and torque [16, 17] averaged along the inner and outer cylinders of Reynolds number. The objective is also the examination how the influence of the end-wall boundary conditions on the flow structure depends on the curvature of cylinders, parameterized in the paper by η. These results are discussed in the light of the data obtained from correlation formulas proposed by Lopez et al. [2] for an infinitely long cavity and for the cavity of aspect ratio $\Gamma = 10$. The analysis is supposed to show the possibilities of using the existing data obtained for the infinitely long cylinders to predict processes in the cavities of small Γ closed by the end-walls.

The outline of the paper is as follows: the mathematical and numerical models are given in section 2. The flow structure, the radial profiles of the mean angular velocity and momentum, and the radial profiles of the dimensionless temperature obtained for cavity of $\Gamma = 3.76$, $\eta = 0.82$ are presented in section 3.1. The distributions of the Nusselt number and torque along the inner and outer cylinders, as well as, the dependence of the averaged values from Re are analyzed in section 3.2. In section 4 the flow structure obtained for the isothermal and the non-isothermal flow cases of $\Gamma = 3.76$, $\eta = 0.375$ are discussed. The conclusions are given in section 5.

2. The mathematical and numerical approaches

We consider the flow with heat transfer between two concentric cylinders of aspect ratio $\Gamma = 3.76$ and radii ratios 0.82 and 0.375 closed by end-walls. The inner cylinder of radius R_1 and the bottom disk rotates at a constant angular velocity Ω, while, the outer cylinder of radius R_2 and the top disk are at rest. The flow is described by the Navier-Stokes, continuity and energy equations written in a cylindrical coordinate system (R, φ, Z), with respect to rotating frame of reference:

$$\nabla \cdot \mathrm{V} = 0 \tag{1}$$

$$\rho \frac{\partial \mathrm{V}}{\partial t} + \rho(\mathrm{V} \cdot \nabla)\mathrm{V} + \rho\Omega \times (\Omega \times R) + 2\rho\Omega \times \mathrm{V} = -\nabla P + \mu \Delta \mathrm{V} \tag{2}$$

$$\frac{\partial T}{\partial t} + (\mathrm{V} \cdot \nabla)T = a\Delta T \tag{3}$$

where t is time, R is radius, P is pressure, ρ is density, **V** is the velocity vector, a is the thermal diffusivity and ν is the dynamic viscosity. The dimensionless axial and radial coordinates are: $z = Z/(H/2)$, $z \in [-1, 1]$, $r = [2R - (R_2 + R_1)]/(R_2 - R_1)$, $r \in [-1, 1]$. The velocity vector components in radial, azimuthal and axial directions are depicted by U, V and W, respectively, T is temperature. The

Boussinesq approximation is used to take into account the buoyancy effects induced by the involved body forces $\rho=\rho_r[1-\beta(T-T_1)]$, where $\beta=-1/\rho_r\cdot(\partial\rho/\partial T)_P$. For validity of Boussinesq approximation the thermal Rossby number $B=\beta(T_2-T_1)]$ is limited to $B\le 0.1$. The Prandtl number is equal to 0.71. The velocity components are normalized as follows: $u=U/\Omega R_2$, $v=V/\Omega R_2$, $w=W/\Omega R_2$. The dimensionless temperature is defined in the following way: $\vartheta=(T-T_1)/(T_2-T_1)$. The no-slip boundary conditions are applied to all rigid walls $(u=w=0)$. For the azimuthal velocity component the boundary conditions are: $v=0$ on the rotating inner cylinder and rotating bottom disk, and $v=-(Rm+r)/(Rm+1)$ on the stationary outer cylinder and stationary top disk. The bottom disk and the outer cylinder are heated $\vartheta=1$, and the top disk and the inner cylinder are cooled $\vartheta=0$. In order to eliminate singularities of the azimuthal velocity components at the junctions between the rotating and stationary walls, the azimuthal velocity is regularized by exponential profiles. The exponential profiles are used also for temperature at the junctions between the heated and cooled walls.

The numerical simulations (DNS/SVV) are based on a pseudo-spectral Chebyshev-Fourier-Galerkin collocation approximation. In time approximation we use a second-order semi-implicit scheme, which combines an implicit treatment of the diffusive term and an explicit Adams–Bashforth scheme for the non-linear convective terms. In the non-homogeneous radial and axial directions we use Chebyshev polynomials with the Gauss–Lobatto distributions to ensure high accuracy of the solution. Predictor/corrector method is used. All dependent variables i.e. predictors of three velocity components u, v and w, predictor of pressure and temperature, and corrector for pressure are obtained by solving Helmholtz equation [18, 19, 20].

For higher Reynolds numbers the SVV method is used. In this method an artificial viscous operator is added to Laplace operator to stabilize the computational process, [20]. The SVV operator is sufficiently effective to suppress Gibbs oscillations and simultaneously the SVV does not affect the solution accuracy**.** More detailed information about SVV algorithm can be found in [21, 22, 23]. For the visualization purpose we use the λ_2 criterion. The computations have been performed using mesh of 5-10 million collocation points. The time step is from the range $\delta t=0.01-0.0005$. The verification of the DNS/SVV algorithm has been done in [22, 23].

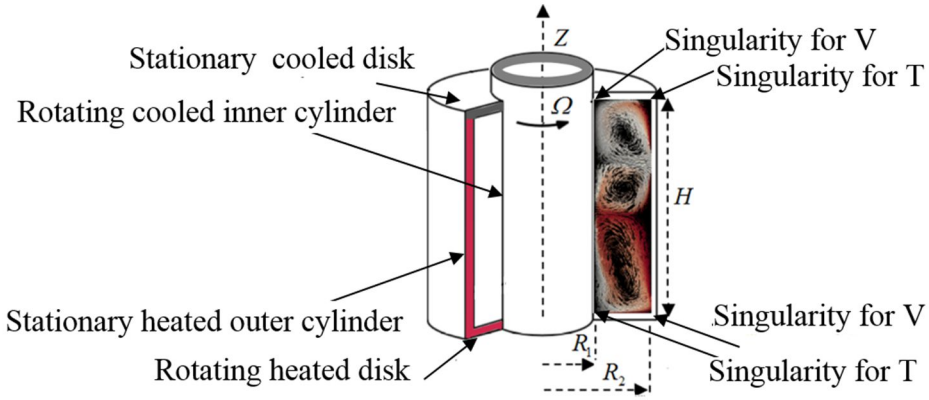

Figure 1. Schematic picture of the Taylor-Couette flow.

3. Selected results obtained for the flow case of $\Gamma = 3.76$, $\eta = 0.82$

3.1. The flow structure

In the cavity of aspect ratio $\Gamma = 3.76$ and radii ratio $\eta = 0.82$ with the heated bottom rotating disk and the stationary outer cylinder the Taylor-Couette vortices are formed at Re=80 above which three vortices in the meridian section are created, figure 3a. We observe the inflow jet along the top stationary end-wall and the outflow jet along the rotating bottom disk. The transition to unsteadiness

takes place at Re = 916.7 (the critical Re of transition to unsteadiness for the isothermal flow case equals Re = 959). At Re = 916.7 we observe 10 spiral vortices (figure 2a) rising from the rotating bottom disk of the azimuthal wave lengths $\lambda_a/(H/2) = 1.7$ (in the isothermal flow case we observe 15 spirals of the azimuthal wave length $\lambda_a/(H/2) = 1.13$). The spirals occupy a large part of cavity and influence the total flow structure. We have traced the azimuthal velocity component in time in the middle section near the top disk, which allows us to characterize the growing disturbances, figure 2b.

Figures 3b, 3c, 3d and 3e show the axial profiles of the dimensionless temperature $<\vartheta>_{t,\varphi}$, the azimuthal velocity component $<v>_{t,\varphi}$, the turbulent heat flux components $<\vartheta'\vartheta'>_{t,\varphi}$ and $<\vartheta'v'>_{t,\varphi}$ obtained in the middle section of cavity ($<\ldots>_{t,\varphi}$ stands for values averaged in time and in azimuthal direction). The meridian flow colored by the dimensionless temperature (figure 3a) allows for correlation between the flow structure and the presented axial profiles. The axial profiles of $<v>_{t,\varphi}$, and $<\vartheta>_{t,\varphi}$ clearly show the existence of two boundary layers at the bottom and top disks. We can see that all extreme values of the presented parameters are connected with the location of the inflow and outflow jets. We observe particularly large peaks in the axial profiles of the turbulent heat flux components $<\vartheta'\vartheta'>_{t,\varphi}$ and $<\vartheta'v'>_{t,\varphi}$.

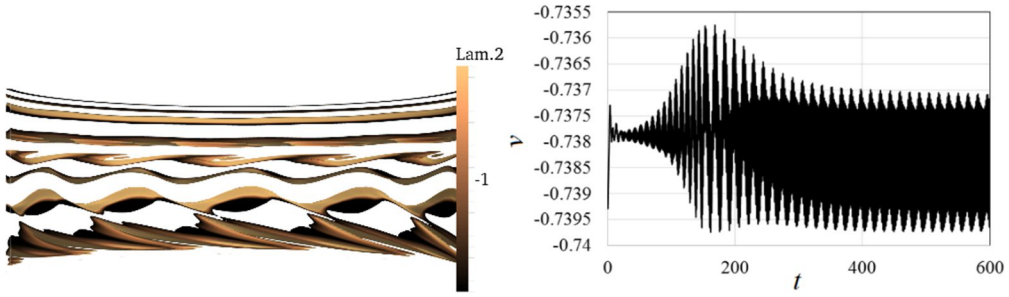

a) b)

Figure 2. The λ_2 iso-surfaces along the cylindrical surface near the inner cylinder (a), v = f(t) obtained in the middle section, r = 0. Re = 916.7, $\Gamma = 3.76$, $\eta = 0.82$, B = 0.1.

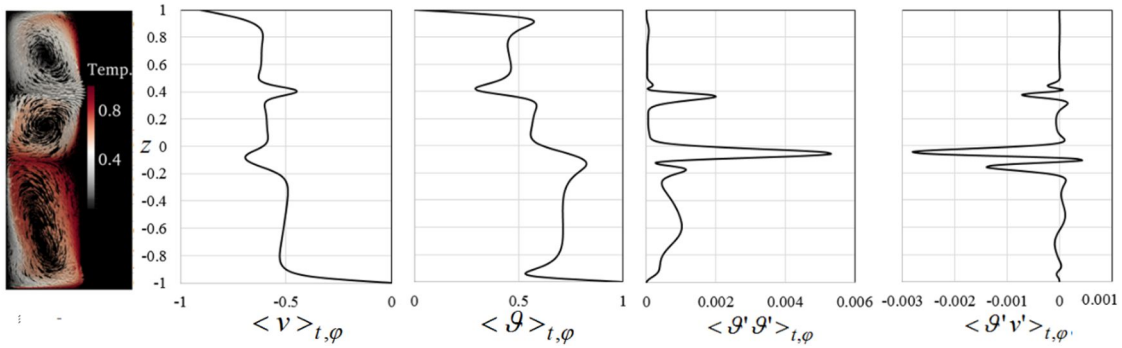

a) b) c) d) e)

Figure 3. The meridian flow structure (a), the axial profiles of: the azimuthal velocity component $<v>_{t,\varphi}$ (b), the dimensionless temperature $<\vartheta>_{t,\varphi}$ (c), the components of heat flux tensor $<\vartheta'\vartheta'>_{t,\varphi}$ (d) and $<\vartheta'v'>_{t,\varphi}$ (e). $\Gamma = 3.76$, $\eta = 0.82$, B = 0.1.

Figure 4 presents the radial profiles of the dimensionless temperature $<\vartheta>_{A(R),t}$, the angular velocity $<(V/R)/(V/R)_1>_{A(R),t}$ and the angular momentum $<(VR)/(VR)_1>_{A(R),t}$ normalized but its value at the inner cylinder ($<\ldots>_{A(R),\varphi}$ stands for time and cylindrical surfaces average). The angular momentum (AM) and the angular velocity profiles (AV) are obtained for the isothermal (B = 0) and non-isothermal fluid (B = 0.1), Re = 1779. From figure 4b we can see that the heating of the rotating disk and the outer cylinder results in the decreasing of $<(V/R)/(V/R)_1>_{A(R),t}$ and of $<(VR)/(VR)_1>_{A(R),t}$ in the central part of the cavity, in comparison to the isothermal flow case (B =

0). This may be due to the fact that with increasing fluid temperature near the rotating disk the density of fluid decreases and so does the centrifugal force. The inverse effect is obtained by increasing Re.

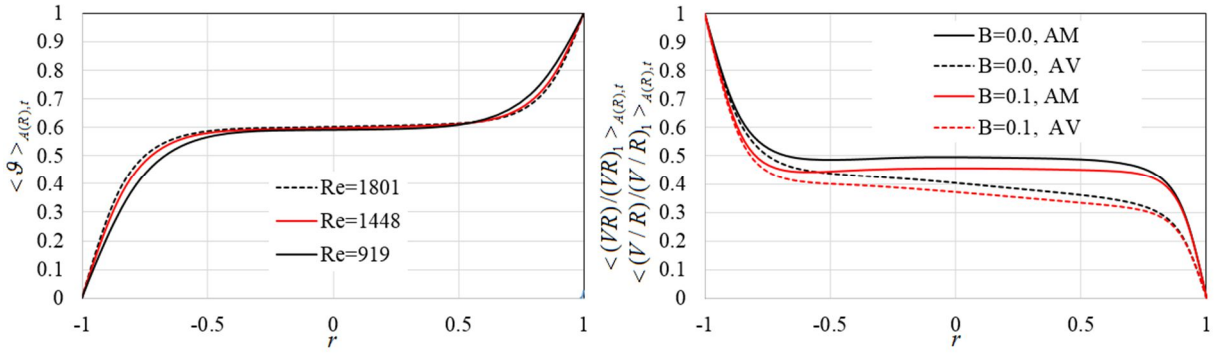

Figure 4. The radial profiles: of the dimensionless temperature, B = 0.1 (a), of the angular velocity and the angular momentum, B = 0.1 and B = 0.0 (b). Re = 1779. $\Gamma = 3.76$, $\eta = 0.82$.

3.2. Distributions of Nusselt number and torque

The heat transfer across the gap is characterized by the distributions of Nusselt number along the inner cylinder and the outer one. The local Nusselt number is obtained in the following way $Nu_{local} = (R_2 - R_1)\alpha / \lambda$, where α ($\alpha = -\lambda(\partial T / \partial R)/(T_2 - T_1)$) is a heat transfer coefficient and λ is a thermal conductivity; the average value is depicted by Nu. Following [16, 17] we also analyze the distributions of the local transverse angular momentum current $j^{\omega} = < R^3[UV/R - \nu\partial(V/R)/\partial R] >_{t,\varphi}$ and, after averaging, in axial direction, its mean value $J^{\omega} = < R^3[UV/R - \nu\partial(V/R)/\partial R] >_{A(R),\varphi}$. The mean J^{ω} is normalized by its laminar value $Nu^{\omega} = J^{\omega} / J^{\omega}_{lam}$, [16]. In [16] the authors showed theoretically that the mean current Nu^{ω} is independent of radius in the infinitely long cavity.

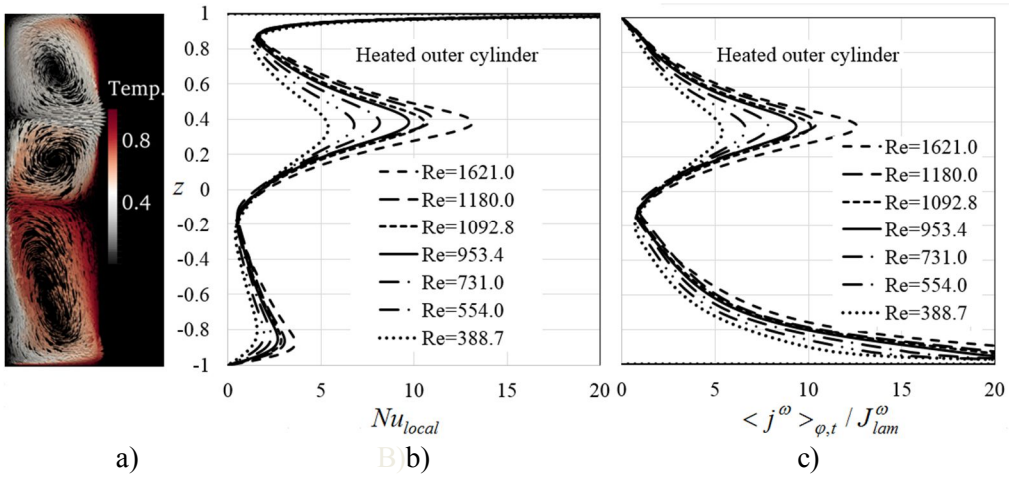

Figure 5. a) The meridian flow, b) Nu_{local} as a function of z, c) $< j^{\omega} >_{\varphi,t} / J^{\omega}_{lam}$ as a function of z, the outer cylinder. B = 0.1, $\Gamma = 3.76$, $\eta = 0.82$.

In figure 5 we analyze the axial distributions of the local Nusselt number Nu_{local} (figure 5b) and $< j^{\omega} >_{\varphi,t} / J^{\omega}_{lam}$ (figure 5c) obtained along the outer cylinder for different Re. We can see that the peak values of Nu_{local} are connected with the outflow jets. The peak value at the top disk (figure 5b) is connected with the singularity of temperature at the junction between the heated outer cylinder and the

cooled top disk. The extreme values of $< j^{\omega} >_{\varphi,t} / J^{\omega}_{lam}$ are observed at the bottom disk (such large value is partly due to the singularity of the azimuthal velocity component at the junction between the rotating bottom disk and the stationary outer cylinder). The remaining peak of $< j^{\omega} >_{\varphi,t} / J^{\omega}_{lam}$ is located at z = 0.4. Along the inner cylinder the peak values of Nu_{local} and $< j^{\omega} >_{\varphi,t} / J^{\omega}_{lam}$ are connected with the inflow jets. We observe the similarity between the axial profiles of Nu_{local} and $< j^{\omega} >_{\varphi,t} / J^{\omega}_{lam}$ in the central part of cavity (both in their shape and values).

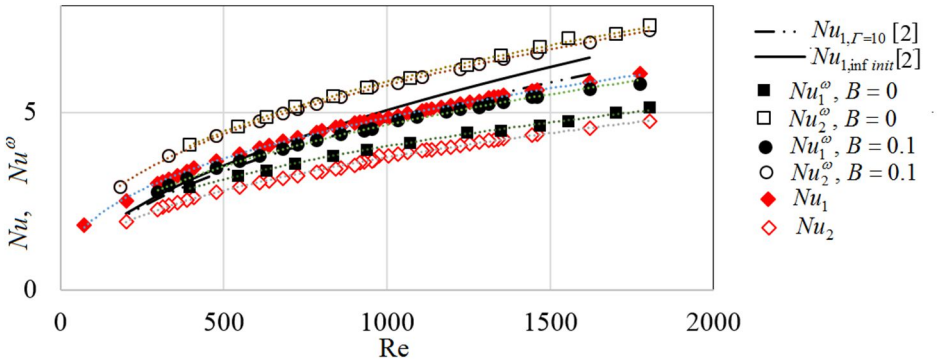

Figure 6. The Nusselt number Nu and Nu^{ω} as a function of Reynolds number with trend lines, ($\Gamma = 3.76,\ \eta = 0.82$), comparison with the results obtained in [2].

In figure 6 we summarize the results by presenting the averaged values Nu and Nu^{ω} as a function of Re. The averaged values are obtained at the inner cylinder (depicted by 1, $Nu_1, Nu^{\omega}{}_1$) and at the outer cylinder (depicted by 2, $Nu_2, Nu^{\omega}{}_2$). The results are compared with the data obtained from the correlation formula $Nu_1 = 0.13\,\mathrm{Re}^{0.53}$ proposed in the paper [2], where the authors investigated numerically (DNS) the flow in infinitely long cavity with the periodicity condition in axial direction (cavity with a heated rotating inner cylinder, a cooled stationary outer one, $\eta = 0.5$, Pr = 0.71, Ra = 1420, [2]). They also performed simulation in the cavity of $\Gamma = 10$ with the no-slip velocity condition at the end-walls and they proposed the following formula $Nu_1 = 0.14\,\mathrm{Re}^{0.51}$ for this flow case. From figure 6 we can see that our results agree with the data obtained from $Nu_1 = 0.14\,\mathrm{Re}^{0.51}$ ($\Gamma = 10$), in spite of differences in thermal boundary conditions. The differences between results are larger, for Re > 1000, when we compare our results with the data [2] obtained with the periodicity condition in axial direction. The Nusselt numbers at the outer cylinder Nu_2 are smaller in comparison to Nu_1, approximately $Nu_2 / Nu_1 = 0.78$. From figure 6 we can also see that our Nusselt number distribution Nu_1 agrees well with the distribution of $Nu^{\omega}{}_1$, and that $Nu^{\omega}{}_2$ is larger than $Nu^{\omega}{}_1$. For Re=1620, B=0.1 we estimate the difference between values $Nu^{\omega}{}_2$ and $Nu^{\omega}{}_1$ as follows: $(Nu_2^{\omega} - Nu_1^{\omega}) / Nu_1^{\omega} = 0.23$. The result shows that in the considered flow cases the influence of the end-wall boundary conditions is large (for infinitely long cylinders $Nu_2^{\omega} = Nu_1^{\omega}$).

4. Selected results obtained for the flow case of $\Gamma = 3.76$, $\eta = 0.375$

In this section we present a comparison of the flow structure obtained with the isothermal and non-isothermal boundary conditions in the cavity of radii ratio $\eta = 0.375$. For the isothermal fluid flow (B = 0) the three-cell Taylor-Couette flow structure is formed at Reynolds number Re = 80. At about Re = 270 the middle vortex is squeezed by the growth of the vortex adjacent to the bottom rotating disk (this process was previously described in [15]). Finally, the steady three-cell structure collapses to a

one-cell structure at the critical Reynolds number Re = 281 via a saddle-node bifurcation. The transition to unsteadiness occurs at Re = 492. Above Re = 492 we observe six spirals of the dimensionless azimuthal wavelength $\lambda_a/(H/2) = 0.6128$, figure 7d.

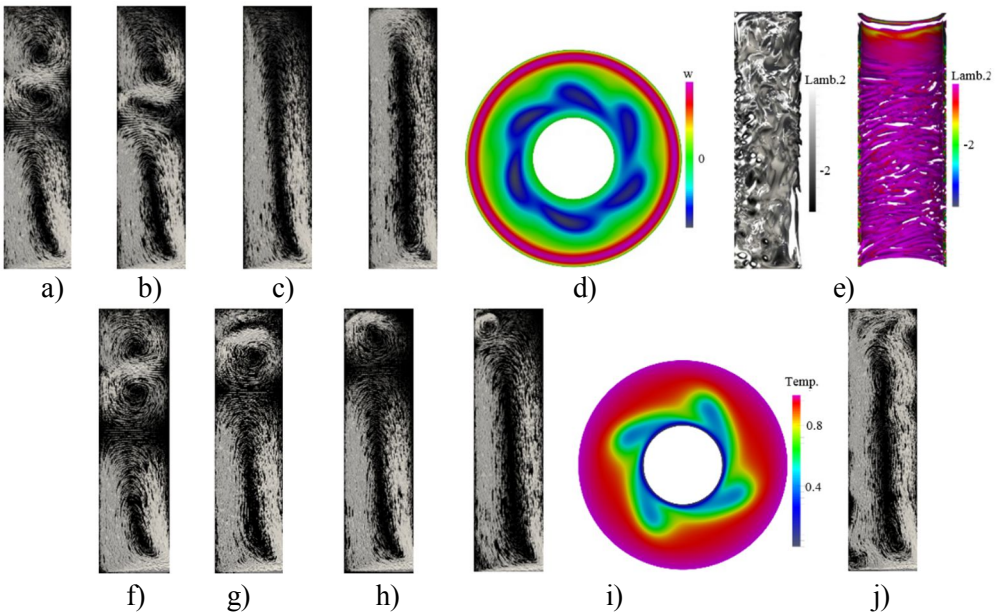

Figure 7. The flow structure obtained for different Re: a) Re = 176, B = 0, b) Re = 270, B = 0, c) Re = 281, B = 0, d) Re = 586, B = 0, e) Re = 4500, B = 0, f) Re = 176, B = 0.1, g) Re = 286, B = 0.1, h) Re = 288, B = 0.1, i) Re = 560, B = 0.1, j) Re = 890.6, B = 0.1. $\Gamma = 3.76$, $\eta = 0.375$.

The same computations have been performed for the thermal Rossby number B=0.1 with the heated outer stationary cylinder and the rotating bottom disk. The use of the non-izothermal boundary conditions changes the procedure of the transition from the three-cell structure to the one-cell structure. Again, the three-cell structure is formed at approximately Re = 80, then at approximately Re = 286 the top vortex is squeezed by the growth of the vortex adjacent to the bottom rotating disk, which results in the appearance of the two-cell structure at Re = 288, figure 7h. The flow is pumped outward along rotating bottom disk in accordance with the boundary condition, and it is pumped radially outward along the stationary top disk in opposite direction to what we can expect from the boundary condition. However, in the corner between the inner rotating cylinder and the stationary top disk there is a very small vortex (hardly visible in figure 7h) which rotates in accordance with the boundary condition. The transition to unsteadiness takes place at Re = 553, above which we observe four spiral vortices. From figures 7f-7i we can see that with the increasing Re the top vortex gradually shrinks and finally the one-cell structure is formed. We can conclude that the use of the non-isothermal boundary conditions delays the formation of the one cell-structure in comparison to the isothermal flow case (and generally slightly weakens the effect of the end-wall boundary conditions). The similar procedure of the transition from the three-cell structure to the one-cell structure we observe in the flow case of $\Gamma = 3.76$, $\eta = 0.524$, B = 0. For higher radii ratios $\eta = 0.756$ and 0.82 the classic Taylor-Couette laminar-turbulent transition takes place.

5. Conclusions

In the paper we investigate, with the use of DNS, the transitional Taylor-Couette flow between the rotating inner cylinder and bottom disk, and the stationary outer cylinder and top disk (the bottom disk and the outer cylinder are heated). The computations have been performed for the cavities of $\Gamma = 3.76$ and different radii ratios $\eta = 0.375$, 0.524, 0.615, 0.756 and 0.821 (in the paper attention is focused on the flow cases of $\eta = 0.375$ and 0.821; B = 0 and 0.1, Pr = 0.71).

For all flow cases we observe the strong effect of the Ekman boundary layers on the flow structure, however, this effect depends on the curvature of cylinders (η). For the flow case of $\eta = 0.375$ (B = 0), the effect of end-walls is so strong that it leads to a rapid transition from the three-cell structure to the one-cell structure. The use of the non-isothermal boundary conditions results in the appearance of an intermediate two-cell structure which delays the transition. The same scenario takes place in the flow case of $\eta = 0.524$. For other values $\eta = 0.756$ and 0.821 we observe the gradual development of the three-cell structure illustrated in section 3.1.

In order to better characterize the influence of the undertaken boundary conditions on the flow we examine the axial distributions of the local transverse angular momentum current $< j^{\omega} >_{\varphi,t} / J^{\omega}_{lam}$ and the distributions of the local Nussent number along the inner and outer cylinders. The comparison shows the similarity between the axial profiles of Nu_{local} and $< j^{\omega} >_{\varphi,t} / J^{\omega}_{lam}$ in the central part of the cavity but we observe large influence of singularities (of temperature and v) on the distributions near the disks. The distributions of the averaged values $Nu^{\omega}{}_2, Nu^{\omega}{}_1, Nu_2, Nu_1$ as a function of Re show that $Nu^{\omega}{}_1$ and Nu_1 take very similar values. Simultaneously, Nu_1 is larger than Nu_2; we estimate the correlation as $Nu_2 / Nu_1 = 0.78$. The comparison with the correlation formula $Nu_1 = 0.14\,\mathrm{Re}^{0.51}$ [2] obtained for $\Gamma = 10$ shows agreement. However, we observe discrepancies for Re > 1000 in comparison to correlation proposed in [2] for infinitely long cavity. The results obtained for $\Gamma = 3.76$ show that in the configuration of such low aspect ratio the influence of the end-walls is very large, particularly for smaller η.

Acknowledgements
The authors are grateful to the Poznań Supercomputing and Networking Center, where the computations have been performed.

References

[1] Fenot M, Bertin Y, Dorignac E and Lalizel G 2011 *Int. J. Thermal Sciences* **50** 7 1138
[2] Lopez J, Marques F and Avila M 2015 *Phys. Fluids* arXiv:1503.06816
[3] Owen J and Rogers R 1995 Research Studies Press Taunton, Somerset, England
[4] Singer P 1984 Semiconductor International 72
[5] Vives C 1988 *Int. J. of Heat and Mass Transfer* **31** 10
[6] Selimefendigil F 2014 *Int. J. of Thermal Sciences* **86** 258
[7] Lopez J, Marques F and Avila M 2013 *J. Fluid Mech*. **737** 56
[8] Poncet S, Haddadi S and Viazzo S 2011 *Int. J. Heat and Fluid Flow* **32** 128
[9] Yoshikawa H, Nagata M and Mutabazi I 2013 *Phys. Fluids* **25** 114104
[10] Sorour M and Coney J 1979 *J. Mech. Eng. Sci*. **21** 403
[11] Lepiller V, Goharzadeh A, Prigent A and Mutabazi I 2008 *The European Physical J.* B 71 445
[12] Ball K and Farouk B 1987 *Int. J. Numer. Meth. Fluids* **7** 857
[13] Ball K and Farouk B 1988 *J. Fluid Mech.* **197** 479
[14] Kuo D and Ball K 1997 *Phys. Fluids* **9** 2872
[15] Mullin T and Blohm C 2001 *Phys. Fluids* **13** 136
[16] Eckhardt B, Grossmann S and Lohse D 2007 *J. Fluid Mech.* **581** 221
[17] Brauckmann H and Eckhardt B 2013 *J. Fluid Mech*. **718**, 398
[18] Tuliszka-Sznitko E, Zieliński A and Majchrowski W 2009 *Int. J. Heat and Fluid Flow* **30** 534
[19] Tuliszka-Sznitko E, Majchrowski W and Kiełczewski K 2012 *Int. J. Heat and Fluid Flow* **35** 52
[20] Tadmor I 1989 *SIAM J. Numerical Analysis* 26 **30** 1989
[21] Severac E and Serre E 2007 *J. Comp. Phys*. **226** 2 1234
[22] Kielczewski K and Tuliszka-Sznitko E 2013 *Arch. Mech*. **65** 527
[23] Tuliszka-Sznitko E and Kielczewski K 2015 *Comp. Method in Science and Tech*. **21** 211